Assimilative Mapping : TS18 Model Error Covariance

Chloe J. Baker, Nathaniel A. Alden, Evan G. Thomas, Simon G. Shepherd

Dartmouth College, Hanover, NH

THAYER SCHOOL OF ENGINEERING AT DARTMOUTH

CEDAR 2022 Workshop

Introduction

❑ The Super Dual Auroral Radar Network (SuperDARN) consists of approximately 40 HF radars which continuously measure plasma parameters in the ionosphere including line of sight (LOS) velocity.

❑ Many climatological models are available to describe convection under certain conditions such as solar wind, IMF, and geomagnetic activity. Several, such as those referred to as the RG96, CS10, and TS18 models, were developed using SuperDARN observations.

❑ These models describe large-scale patterns and **do not** incorporate instantaneous data when providing a fit for a given set of external parameters.

❑ To determine a global plasma convection pattern *at a particular time,* assimilative techniques attempt to appropriately combine climatological models with instantaneous data. For example, the "Map Potential" procedure [*Ruohoniemi and Baker,* 1998] combines available SuperDARN LOS data with the background model of choice using an error-weighted least squares method.

❑ An alternative, the SuperDARN Assimilative Mapping (SAM) technique, was successfully applied to the CS10 model [*Cousins et al.,* 2013b]. Assimilative mapping is a a popular technique used in modeling where there exists spatially sparse data with substantial temporal coverage. Assimilative Mapping seeks to optimally combine climatological maps and new data using the covariance of the error of each.

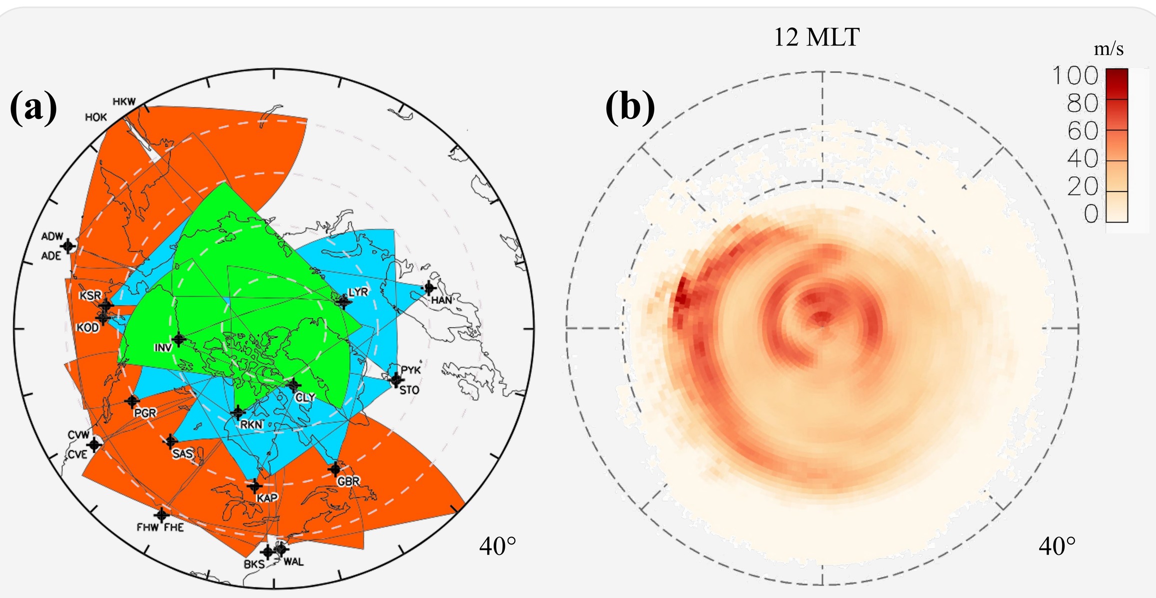

Figure 1: (a) Northern Hemisphere SuperDARN FOVs showing polar latitudes (green) and mid-latitudes (orange) expansions since the CS10 model [*Thomas and Shepherd,* 2018] (b) The average difference in residuals (data - model) between the TS18 [*Thomas and Shepherd,* 2018] and CS10 models for strong Southwards (< -5 nT) IMF B_z conditions for 2014 (MLT/magnetic latitude)

❑ Over the past decade the number and coverage of radars has improved significantly as shown in figure 1. Such expansion warrants a reapplication to the TS18 model (which incorporates these new radars and data).

Preliminary results

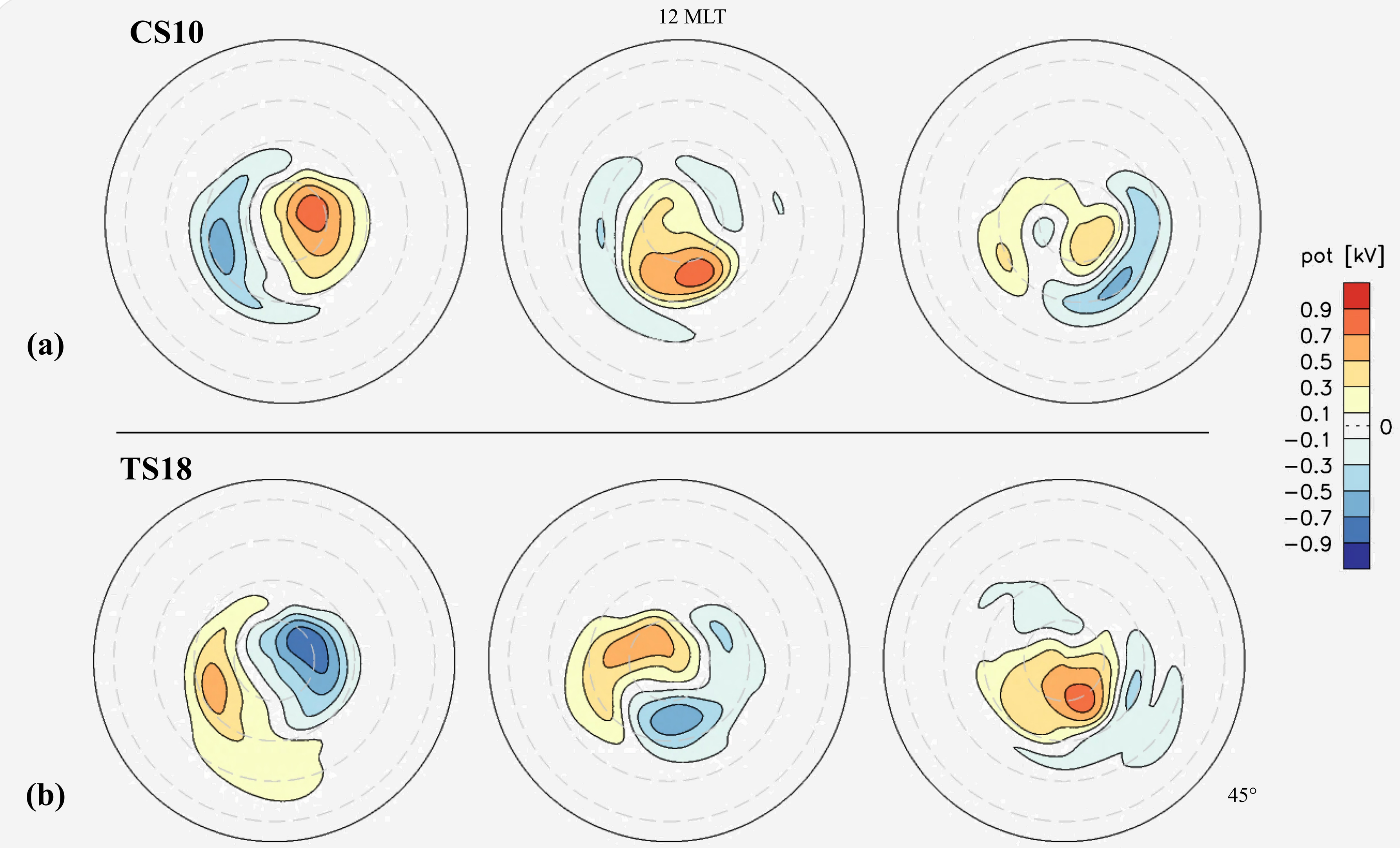

Figure 4: (a) First three normalized principal components (EOFs) for the CS10 model (b) For the latest model, the TS18. These are a sample constructed from 500 random time steps in 2010-2016 for illustrative and investigative purposes only.

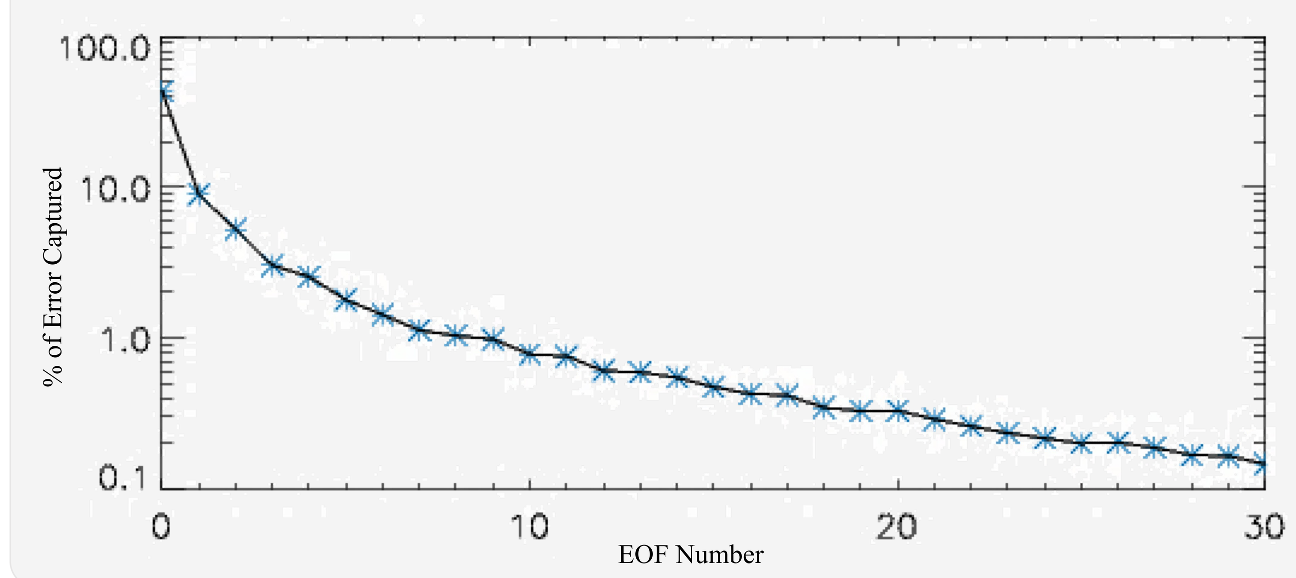

Figure 5: Percent of error captured by the TS18 model (0), and by EOFs 1-30. EOFs are constructed from the same 500 random time steps in 2010-2016 used in figure4.

❑ Figure 4 illustrates the differences between the first three EOFs characterizing the residuals for the CS10 (a) and the TS18 (b) models. The sign on each EOF is arbitrary as alpha values for any time step can be negative or positive. Both feature a two-cell convection mode of variability followed by other patterns in different orientations. Because these EOFs represent the features of the residuals of the model, their differences affirm the need to calculate a unique covariance matrix for each model used with SAM.

❑ Nearly 60% of the data's variability is captured by the model (indicated by EOF 0 in figure 5), followed by ~9% by the first EOF. Subsequent EOFs account for decreasing amounts of error with the final few each only representing 1-2%.

Methodology

❑ In order to use the TS18 model with the SAM technique the error covariance matrix of the TS18 model must be determined. Following *Matsuo et al.*, [2002], the residuals between the observations and the vectors predicted by the model are fitted to an orthonormal basis, resulting in a set of 30 Empirical Orthogonal Functions (EOFs).

❑ EOFs are represented in terms of coefficient vectors (**α** and ***β***) which minimize the cost function below. EOFs are determined sequentially using fixed-point iteration, subtracting the resulting EOF, and repeating.

$$C^{(\nu)} = \sum_{j}^{J} \sum_{i}^{L} \frac{1}{\epsilon_{ij}^2} \left[Y_{ij}^{(\nu)} - \alpha_j^{(\nu)} \sum_{k=1}^{K} \beta_k^{(\nu)} Z_{kij} \right]^2$$

❑ Where the indices ***i*** and ***j*** indicate spatial and temporal dimensions, ***Y*** is the observation residual (with weight ϵ), and $\boldsymbol{Z_{ijk}}$ is the corresponding component of the $\boldsymbol{k^{th}}$ basis function in the obs. LOS direction.

❑ Ultimately, an optimal set of EOF coefficients is found using $\boldsymbol{P_b}$, the background model error covariance matrix defined below for ***Q*** EOFs.

$$P_b^{nm} = \frac{1}{J-1} \sum_{j=1}^{J} \left[\alpha_j^n \alpha_j^m \right], m = 1...Q, n = 1...Q$$

❑ The basis used here [figure 2] is the set of the top ~60 (***K***) principal components found by *Richmond and Kamide,* [1988] for a similar application. They are scaled to 40° and smoothed at lower latitudes [*Cousins et al.,* 2013a; and *Matsuo et al.*, 2002].

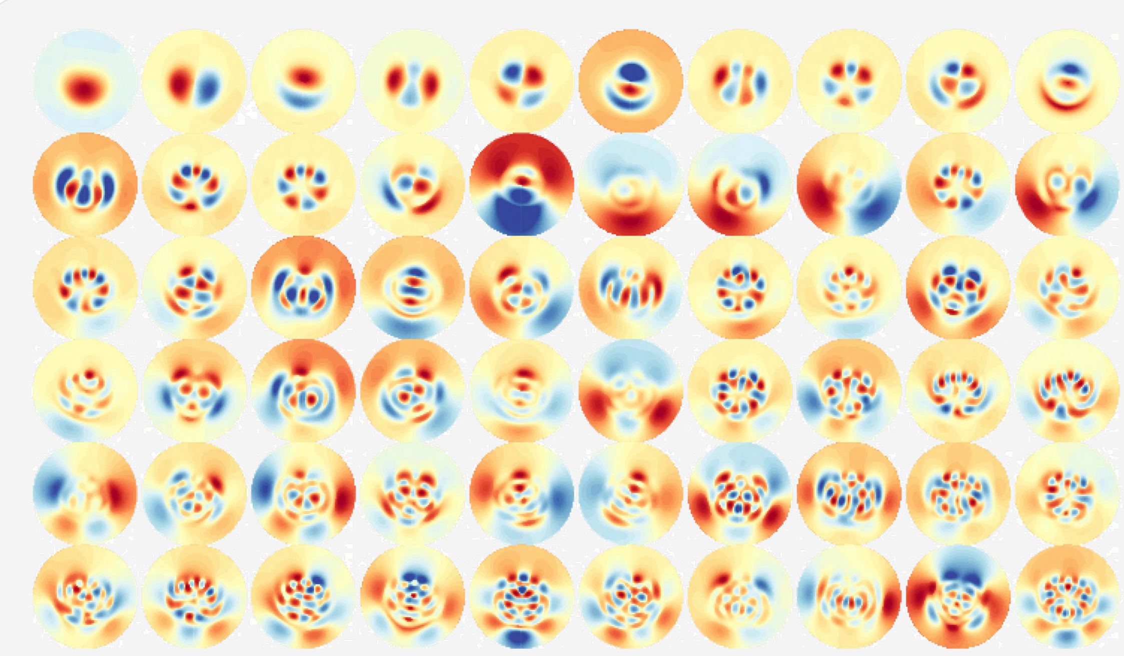

Figure 2: Principal components found by Richmond and Kamide [1988], combining a larger set (244) of harmonic associated Legendre polynomials to represent the dominant modes of variability in plasma convection.

❑ Zero magnitude vectors are added at lower latitudes to constrain the solution where there is no data and the potential is known to be low. The impact of these vectors is seen in figure 3.

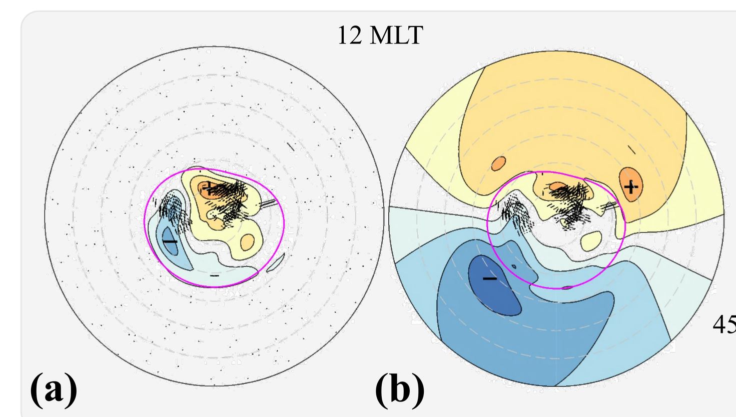

Figure 3: (a) Sample first EOF with low latitude constraint vs. (b) without. Velocity vectors and Max/Min potentials are marked in black.

Summary & Future Work

❑ We are working to construct the EOF set and covariance matrix, which includes tuning the weight and placement of low latitude constraints, selecting data filters, and investigating orthogonalization methods.

❑ These assimilative techniques will be compared across background models and ionospheric conditions. The accuracy of local and global fits will be evaluated for different geophysical conditions.

References

❑ Cousins, E. D. P., Matsuo, T., and Richmond, A. D. (2013), Mesoscale and large-scale variability in high-latitude ionospheric convection: Dominant modes and spatial/temporal coherence, J. Geophys. Res. Space Physics, 118, 7895– 7904

❑Cousins, E. D. P., Matsuo, T., and Richmond, A. D. (2013), SuperDARN assimilative mapping, J. Geophys. Res. Space Physics, 118, 7954– 7962

❑ Matsuo, T., Richmond, A. D., and Nychka, D. W., Modes of high-latitude electric field variability derived from DE-2 measurements: Empirical Orthogonal Function (EOF) analysis, Geophys. Res. Lett., 29(7)

❑Richmond, A. D., and Y. Kamide (1988), Mapping electrodynamic features of the high-latitude ionosphere from localized observations: Technique, J. Geophys. Res., 93, 5741

❑Ruohoniemi, J. M., and K. B. Baker (1998), Large-scale imaging of high-latitude convection with Super Dual Auroral Radar Network HF radar observations, J. Geophys. Res., 103, 20,797

❑ Thomas, E. G., & Shepherd, S. G. (2018). Statistical patterns of ionospheric convection derived from mid-latitude, high-latitude, and polar SuperDARN HF radar observations. Journal of Geophysical Research: Space Physics, 123, 3196– 3216

Contact: *chloe.j.baker.th@dartmouth.edu*

This research is funded by NSF grant AGS-1934997 and NASA grant 80NSSC20M0051